Simultaneously-recorded cholinergic axons and cortical acetylcholine are highly correlated with pupil size and locomotion under spontaneous conditions

Erin Neyhart[1], Na Zhou[1], Brandon R. Munn[2,3], Robert G. Law[1], Cameron Smith[1], Zakir H. Mridha[1], Francisco A. Blanco[1], Guochuan Li[4,5,6], Yulong Li[4,5,6], Matthew J. McGinley[1], James M. Shine[2,3], Jacob Reimer[1]

1. Neuroscience Department, Baylor College of Medicine, Houston, Texas, USA
2. Brain and Mind Centre, School of Medical Sciences, Faculty of Medicine and Health, The University of Sydney, Australia
3. Complex Systems Group, School of Physics, Faculty of Science, The University of Sydney, Australia
4. State Key Laboratory of Membrane Biology, Peking University School of Life Sciences, Beijing, China
5. PKU–IDG/McGovern Institute for Brain Research, Beijing, China
6. Peking–Tsinghua Center for Life Sciences, Academy for Advanced Interdisciplinary Studies, Peking University, Beijing, China

Abstract

Even under spontaneous conditions and in the absence of changing environmental demands, awake animals alternate between moments of increased alertness and moments of torpor or disengagement. These changes in brain state can occur rapidly, on a timescale of seconds, and may be correlated with overt changes in exploratory behaviors (walking and whisking) or they may be more covert, with no external correlates except for changes in pupil size. Neuromodulators such as acetylcholine (ACh) are thought to play an important role in driving these spontaneous state transitions, and cholinergic activity in cortex has been monitored via calcium imaging of cholinergic axons and with new genetically-encoded fluorescent neuromodulator sensors. Here, we perform the first simultaneous imaging of sensors and axons in vivo, to examine the spatiotemporal properties of cortical acetylcholine (ACh) release during spontaneous changes in behavioral state. As has been previously reported, periods of locomotion were accompanied by large increases in ACh levels across the dorsal cortex, and pupil size tracked smaller, more rapid changes in ACh during periods of quiescence. We observed a high correlation between simultaneously-recorded basal forebrain axon activity and neuromodulator sensor fluorescence. Consistent with volume transmission of ACh, increases in axon activity resulted in increases in local ACh levels that fell off with the distance from the nearest axon. GRAB-ACh fluorescence could be accurately predicted from axonal activity alone, providing the first validation that neuromodulator axon activity is a reliable proxy for nearby neuromodulator levels. To more precisely understand the temporal kinetics of ACh, we applied a deconvolution approach to account for the kinetics of the ACh sensor. Deconvolution of fluorescence traces emphasized the rapid clearance of ACh, especially for smaller transients outside of running periods. Finally, we trained a predictive model of ACh fluctuations from the combination of pupil size and running speed; this model performed better than using either variable alone, and generalized well to unseen data. Overall, these results contribute to a growing understanding of the precise timing and spatial characteristics of cortical ACh during fast brain state transitions under spontaneous conditions.

INTRODUCTION

While animals are awake, their level of alertness and engagement with the world varies from moment to moment, and these spontaneous state changes can occur on fast timescales that are correlated with behavior and rapidly shift neural activity from one mode to another. For example, in mouse visual cortex, neurons are depolarized and membrane potential variability is reduced during exploratory periods of locomotion and whisking[1–4], visual responsiveness is enhanced[1,3–7], and population noise and signal correlation are reduced[8,9]. Outside of these movement periods (i.e. during "quiet wakefulness") there are also smaller changes in state with similar neural correlates, including a depolarized and less variable membrane potential, reduced amplitude of low-frequency membrane potential oscillations, and increased reliability and selectivity of evoked responses[1,2]. These covert state changes are tracked by dilation and constriction of the pupil that occurs in the absence of any external changes in luminance.

Over the past decade, the mouse has served as an important model for understanding the mechanisms underlying these changes in state, which include neuromodulators[10] such as acetylcholine (ACh)[11–14]. Indeed, activity in cholinergic axons from the basal forebrain (BF) projecting to the cortex is increased during whisking[15–19], locomotion[15–17,20–22], and pupil dilation outside of exploratory periods[20,22], and genetically-encoded ACh sensors have confirmed some of these effects[21,23–26]. Axonal GCaMP activity might not have a straightforward relationship to ACh levels, which depend on local release probabilities and clearance kinetics, as well as the kinetics of the fluorescent sensors themselves. Thus, more work is required to determine if these measurements are equivalent, and to precisely identify when and where ACh is available to influence the cortex during spontaneous fast state changes. Furthermore, the relationship with pupil and locomotion suggests that it should be possible to build a model that uses these easily-measured variables to predict a significant amount of variance in cortical ACh. If this model was shown to generalize well, it could then be employed in other head-fixed mouse experiments to estimate ACh fluctuations in the absence of ground truth data.

We took advantage of recent advances in genetically-encoded fluorescent sensor technology[23] to address these questions. We performed in-vivo benchmarking of GRAB-ACh 3.0 with exogenous application of ACh, and we also characterized the relationship with spontaneous running speed and pupil size fluctuations. We performed the first simultaneous measurements of axons and ACh activity. Reassuringly, we found that ACh is indeed being released when local cholinergic axons are active, the two metrics are tightly correlated, and that on a fine spatial scale, larger ACh increases can be observed nearby cholinergic axons compared to further away. We demonstrate an approach for deconvolving the sensor fluorescence to estimate the underlying changes in ACh levels, and we show that ACh levels can be predicted with relatively high accuracy by a model incorporating pupil and treadmill information.

RESULTS

We used two-photon microscopy to measure ACh activity in the cortex of wild type mice by implanting a cranial window over the visual cortex (VIS) and expressing the genetically-encoded fluorescent ACh sensor GRAB-ACh3.0 via viral injection (Fig. 1a). Although GRAB-ACh3.0 has been benchmarked against varying concentrations of ACh *in vitro*[23], this benchmarking has not been completed *in vivo*. We utilized an approach similar to two-photon-guided patching[1] with a pipette entering through a hole in the coverslip. This technique allowed us to image GRAB-ACh signals in an anesthetized mouse while directly puffing small amounts of ACh into the cortex in the field of view via (Fig. 1b) to measure ACh sensor responses. We observed strong increases in GRAB-ACh fluorescence with 10µM, 100µM, and 1mM ACh concentrations, with the response seeming to plateau at 100µM (Fig. 1c). Puffs of ACh-free cortex buffer and 100µM norepinephrine resulted in mild decreases in GRAB-ACh fluorescence, presumably due to the transient wash-out of endogenous levels of ACh. Interestingly, puffs of 1µM ACh also resulted in a decrease in fluorescence, which might indicate that baseline concentrations of ACh under isoflurane anesthesia in visual cortex are above 1µM. Overall, these experiments directly confirmed that GRAB-ACh fluorescence reflects changes in ACh levels in vivo.

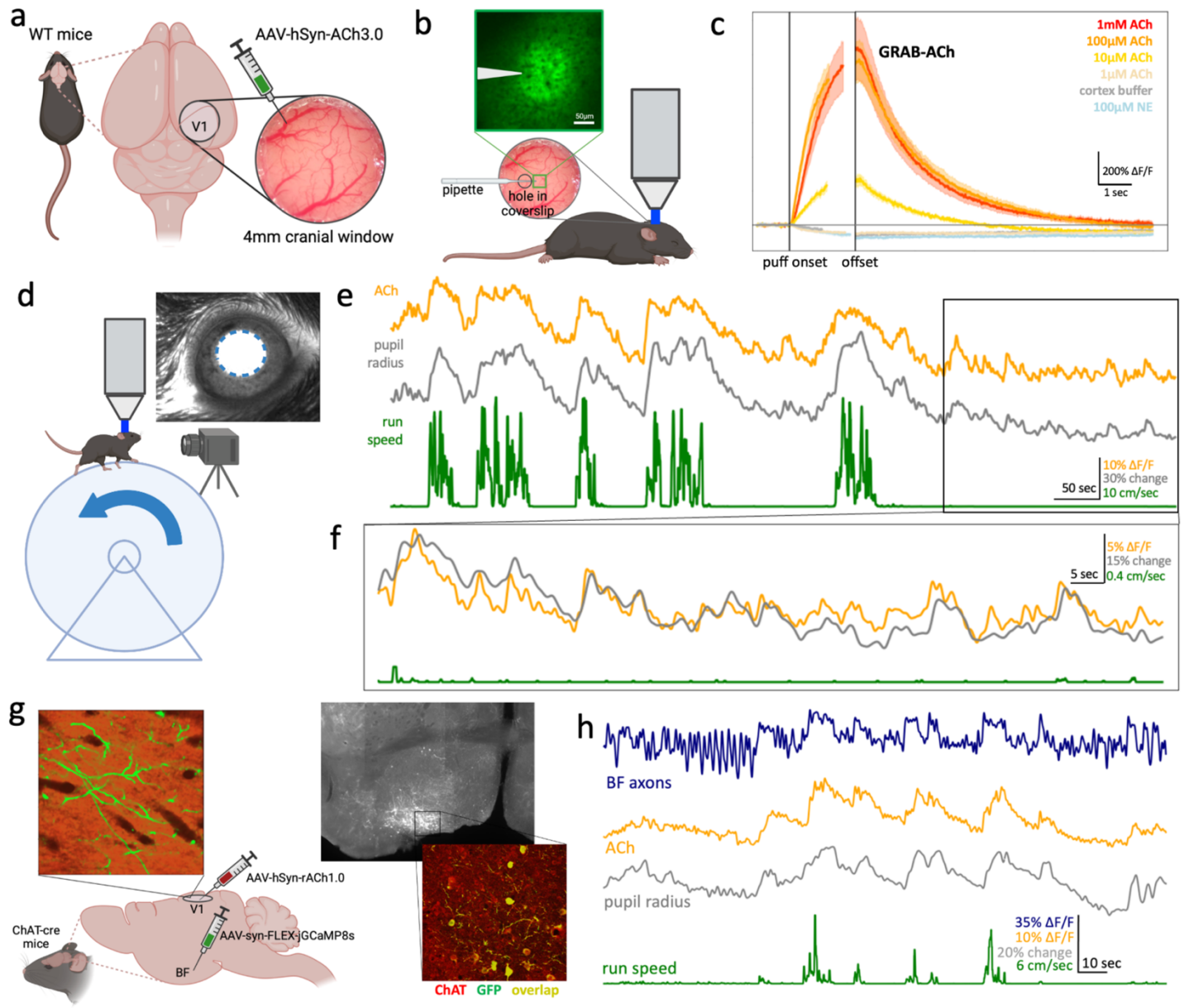

Figure 1: GRAB-ACh activity reveals spontaneous fluctuations in ACh levels which track behavior state and cholinergic axon activity. *a) Animal prep: a cranial window was implanted over the visual cortex of WT mice and GRAB-ACh3.0 was expressed via viral injection. b) For pharmacological validation experiments, a coverslip with a hole was implanted, through which a glass pipette could be inserted. Various concentrations of ACh were puffed onto the cortex while imaging the cortex under general anesthesia. c) Puffs of varying concentrations of ACh resulted in increases in GRAB-ACh fluorescence, while injections of control substances (cortex buffer, NE) resulted in decreases in fluorescence. Puffs of 1μM ACh also resulted in a decrease in fluorescence, consistent with an ambient ACh concentration above 1μM. (N puffs in each group in the order listed = 10, 11, 5, 18, 15, 5). d) Experimental setup for awake, behaving experiments. The mouse was head-fixed on a treadmill in a dark room underneath a two-photon microscope while treadmill speed and a video of the eye were recorded. e) Example traces of spontaneous ACh levels, pupil radius, and run speed while the mouse naturally transitioned between states. Run periods were accompanied by large increases in pupil size and ACh level (as indicated by GRAB-ACh fluorescence). f) A close-up of the example trace in d), highlighting the close correspondence of ACh with spontaneous pupil fluctuations during a period of stillness (quiescence). g) Animal prep for axon imaging experiments. GCaMP8s was expressed in cholinergic axons by viral injection into the HDB of the BF of ChAT-cre mice. A cranial window was implanted over the visual cortex and rACh was expressed via viral injection. Verification of injection sites was subsequently done histologically. h) Example traces of spontaneous axon activity in comparison with simultaneous ACh, pupil radius, and run speed, in which correspondence between all four traces is apparent. Panels a, b, d, and g created with BioRender.com*

We next repeated the measurements we had previously performed relating cholinergic axons to locomotion and pupil under spontaneous conditions, but now using the GRAB-ACh sensor. The mouse was head-fixed on a treadmill and allowed to run freely while the pupil was recorded with a camera, and we simultaneously imaged GRAB-ACh in VIS (Fig. 1d). As expected based on previous studies[15–17,20–22], we observed strong increases in ACh levels which tracked spontaneous locomotion periods and the accompanying large pupil dilations (Fig. 1e). Focusing in on the small dilations which occurred outside of locomotion (i.e., during quiet wakefulness), we

observed a much higher correlation between spontaneous ACh fluctuations and small dilations and constriction of the pupil (Fig. 1f) than expected. This was surprising, as previous work[27], including our own studies recording from ACh axons[20], has emphasized the relationship between pupil and norepinephrine, and we did not expect there to be such a close correspondence between pupil and cortical acetylcholine measured with GRAB-ACh.

This raised the question of whether we could further clarify the dynamic relationship between the activity of cholinergic axons and local ACh levels by measuring them simultaneously. While neuromodulator axon activity and release have been measured simultaneously in vitro[28], to our knowledge this experiment has not been performed in vivo for any neuromodulator. We expressed FLEX-GCaMP8s in cholinergic axons via viral injection into the horizontal diagonal band (HDB) of the BF in ChAT-cre mice, as well as the red ACh sensor rACh1.0 in VIS (Fig. 1g). HDB was chosen due to its preferential projections to VIS[24,29,30], and we used rACh1.0 so that the sensor could be simultaneously imaged with GCaMP activity on red and green emission channels. We observed that BF axon activity was more transient and phasic than ACh activity, but both closely tracked locomotion periods and pupil size (Fig. 1h). Thus, cholinergic axon activity is indeed tightly related to local ACh levels in the cortex, validating previous studies that have used axon activity alone to measure cholinergic tone[16,20] and ameliorating concerns about mechanisms that could potentially dissociate axonal action potentials from neuromodulator release[31].

As expected from previous studies[21,23,25,26], ACh levels in VIS increased during running. To define the timing, magnitude, and spatial heterogeneity of this increase, we measured and compared ACh activity during spontaneous running across three cortical areas: VIS, somatosensory cortex (SS), and motor cortex (MO). When aligning ACh activity to all run onsets and offsets, we observed a similar pattern across all three areas: a large increase right before run onset and a slower decline back to baseline after run offset (Fig. 2a). To look at these onsets and offsets more closely, we restricted to isolated running periods with at least 15 seconds of quiet wakefulness before onsets or after offsets. When matching for similar run speeds across areas, ACh activity began to increase around one second before run onset and declined after running with a decay constant of 5-6 seconds (Fig. 2b). The timing of the initial ACh rise (within the first 5 seconds of running) was not dependent on run speed (Fig. 2c). In contrast with a previous study[21], we observed a clear relationship between run speed and the duration and magnitude of ACh changes, with faster and longer run periods leading to larger ACh increases than smaller and shorter run periods (Fig. 2d). Run speed or duration did not have a significant effect on decay time, but larger ACh responses took longer to decay (Fig 2e). To compare ACh response magnitude across cortical areas, we matched run periods by run speed and duration across recordings in VIS, SS, and MO (Fig. 2f), and for these matched run periods we did not observe a significant difference in peak ACh. In summary, we observed the expected rapid increase of ACh preceding running and a slower decrease back to baseline right at run offset; this increase varied by run speed and duration but was relatively homogeneous across cortical areas.

As we have done previously[1,20], we next excluded active periods to focus on the smaller fluctuations in pupil size that occurred outside of running. Some previous studies have found that cholinergic axon activity[20,22] or ACh levels[24] are coherent with and precede changes in pupil size in cortex, while others found that pupil size was in general not a good predictor of cortical ACh activity[16,25]. In our hands, we found that ACh fluctuations during quiet wakefulness were tightly tracked by small pupil dilations (Fig. 3a). When we compared dilation periods of similar magnitude (Fig. 3b), we found that larger dilation periods were accompanied by larger ACh increases, as well as a shorter lag between ACh rise and dilation onset. Comparing dilation periods of similar magnitude across cortical areas (Fig. 3c), our results suggest that dilation-linked ACh increases were both larger and had a shorter lag in VIS than in SS and MO. Thus, cortical ACh levels are correlated with and precede pupil dilation, although the timing of this relationship may be somewhat heterogeneous across areas.

Previous studies have used calcium indicators expressed in axons as a proxy for changes in local ACh levels[15,16,20,22]. However, axon activity may be dissociated from extracellular neuromodulator levels, which depend on release probabilities and clearance kinetics. In order to directly measure the relationship between axon activity and fluctuations in ACh levels, we recorded cholinergic axon activity with GCaMP in the green channel and rACh in the red channel. As we have observed previously, axon activity increased around running

periods. Reassuringly, in our simultaneous recordings, changes in axon activity preceded changes in ACh activity both at the onset and offset of running (Fig. 4a). When we quantified this timing by examining run periods with

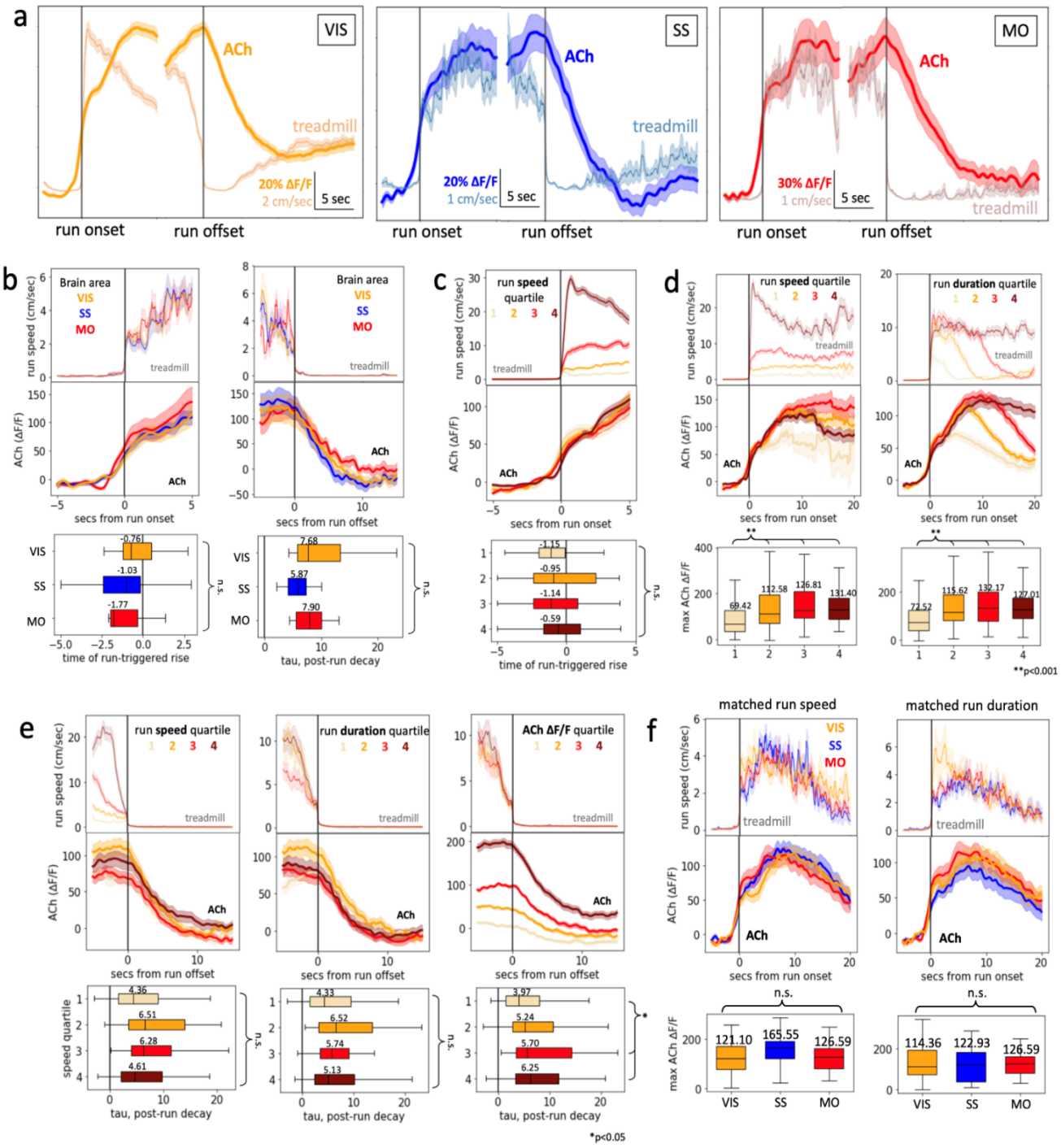

Figure 2: Locomotion is linked to large-scale, slowly decaying increases in ACh which vary by run magnitude and are homogeneous across the dorsal cortex. *a) Run onset- and offset-triggered ACh traces for VIS (n=822), SS (n=33), and MO (n=51). b) Run onsets (n=24 in each area) and offsets (n=14) matched by mean speed in the first/last 5 seconds of running (respectively), and sorted by brain area. Differences between median rise time (p=0.812) and median decay tau (p=0.053) were not significant (Kruskal-Wallis test). c) In VIS, run onset-triggered ACh binned by run speed in the first 5 seconds of running (n=99-100 in each bin; see Supp. Fig. 1 for a breakdown of run speeds). The median time of ACh rise in response to running was not significantly different across areas (p=0.198). d) Run onsets in VIS binned by mean speed in entire run period (n=130 in each in each bin) or total run duration (n=128-129). The median peak ACh ΔF/F was significantly different in both conditions (overall p<0.001), with group 1 being significantly different from groups 2, 3 and 4 (p<0.001). e) Run offsets in VIS (n=62-53 in each bin). Median decay tau (fitted to first 10 seconds after run offset) was not significantly different when binning by mean run speed (overall p=0.050, Kruskal-Wallis test) or run duration (overall p=0.157), but there was an effect of mean ACh ΔF/F in the last 5 seconds of running (overall p=0.043, 1 vs 3 p=0.010; 1 vs. 4 p=0.018). f) Run onsets in matched by mean speed in entire run period (n=130 in each in each bin) or total run duration (n=128-129) and sorted by brain area (n=37 in each area). The median peak ACh ΔF/F was not significantly different between areas in either condition (p=0.137, p=0.472, respectively).*

no running in the 15 seconds before or after running, we found that axon activity began increasing around one second before the rise in ACh, and GRAB-ACh fluorescence decayed about 4 times as slow as the GCaMP axon activity after running, despite the similar off-kinetics of GCaMP and the rACh sensor (Fig. 4b). Although not unexpected, this is the first direct evidence that cholinergic GCaMP activity indeed is correlated with local ACh release, and that ACh remains available for several seconds after axonal activity returns to baseline for large ACh transients.

This led to the question of whether there was an effect of running magnitude on the accompanying axon or ACh activity. Previous evidence for this has been mixed, with one study suggesting that ACh levels do vary by run speed[23] and another study suggesting neither ACh nor axon activity vary by run speed[21]. When binning by average run speed we did not find a significant difference in the magnitude of axon activity, however we again found that faster runs resulted in a larger increase in ACh measured with the fluorescent sensor (Fig 4c). This

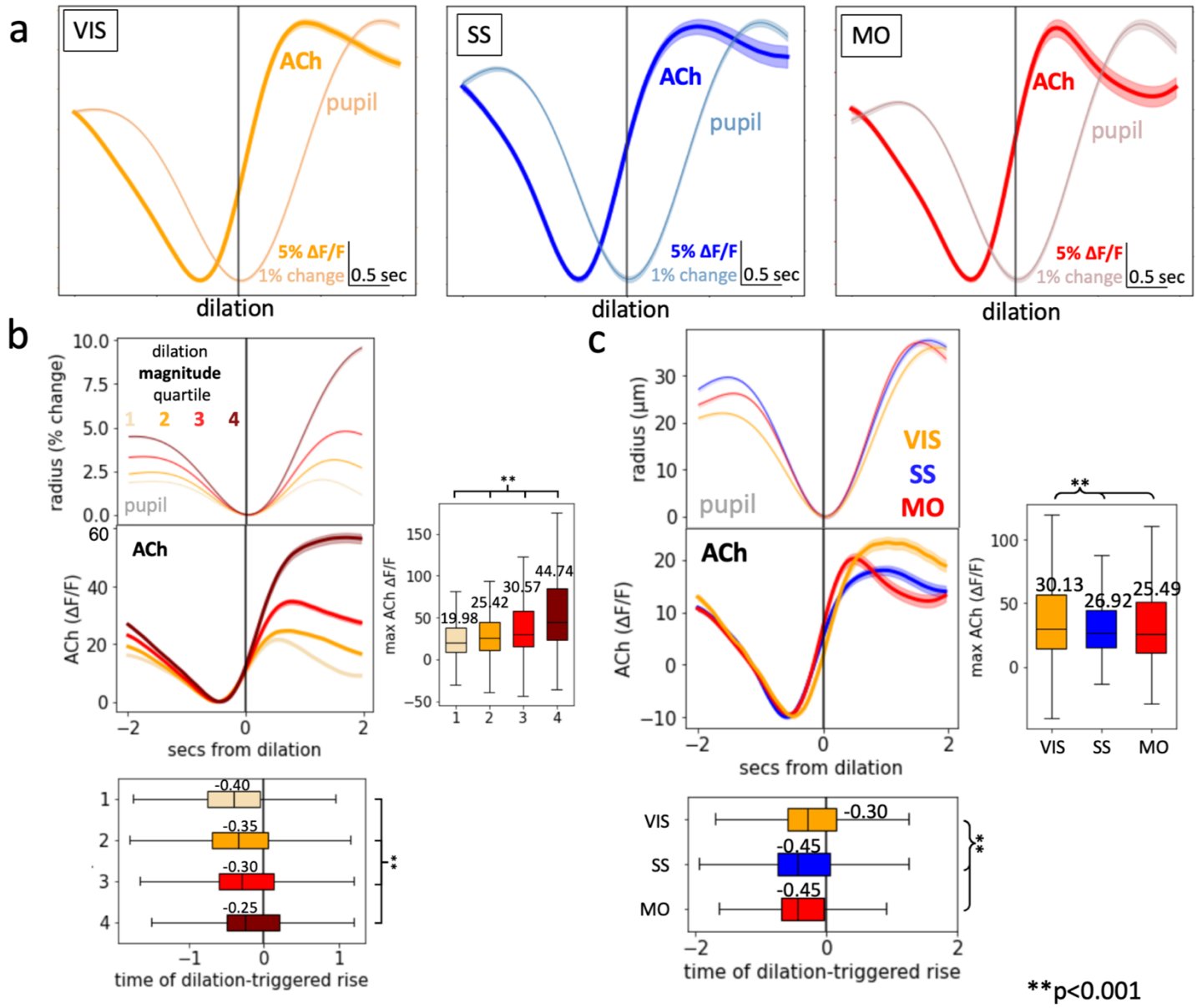

Figure 3: Pupil dilation during quiescence is linked to small-scale, rapid changes in ACh which vary by cortical area*. a) Dilation-triggered ACh traces during stillness for VIS (n=9659), SS (n=1643), and MO (n=1536). b) In VIS, dilation-triggered traces sorted by dilation magnitude (n=2414-2415 in each bin). Median time of dilation-triggered ACh rise was significantly different between bins (overall p<0.001, all pairwise comparisons p<0.001, Kruskal-Wallis test). Median peak ACh ΔF/F was also significantly different between bins (overall p<0.001, all pairwise comparisons p<0.001). c) Dilation-triggered traces matched by dilation magnitude for VIS), SS, and MO (n=1536 for each area). Median time of dilation-triggered ACh rise was significantly closer to dilation in VIS (overall p<0.001, VIS vs SS and VIS vs MO p<0.001, Kruskal-Wallis test). Median peak ACh ΔF/F was also significantly higher in VIS (overall p<0.001, VIS vs SS and VIS vs MO p<0.001).*

result runs counter to the expectation that larger ACh increases during faster running periods must be accompanied by a commensurate increase in GCaMP axonal activity. We found a similar pattern when binning by run duration: only the shortest runs resulted in lower magnitude axon activity, but GRAB-ACh activity was significantly higher as run durations got longer (Fig. 4d). Interestingly, we noticed that the relative timing of these

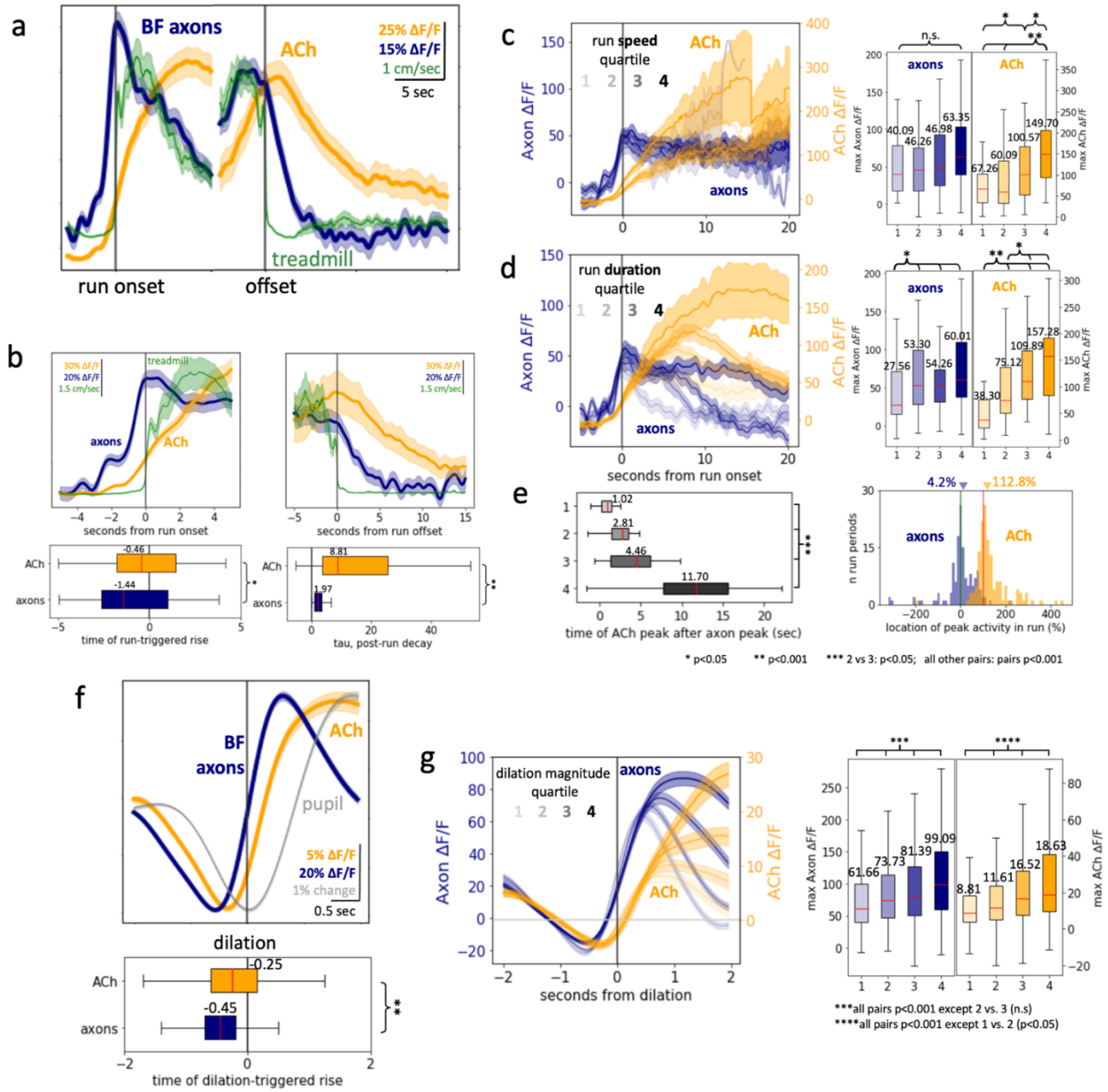

Figure 4: Cholinergic axon activity measured with GCaMP is accompanied by increases in local GRAB-ACh levels which precede locomotion onset and pupil dilation. *a) Run onset- and offset-triggered ACh and axon traces (n=260 run periods). b) Traces with no running in the 15 seconds before or after running, aligned to run onset and offset. Axon activity began to increase significantly sooner before running than ACh activity (n=104 run onsets, p=0.024, Kruskal-Wallis test). Median axon decay tau was also significantly faster for axon activity than ACh activity (n=38 run offsets, p<0.001). c) Run onset-triggered ACh and axon activity binned by mean run speed (n=42 run periods). Median peak axon ΔF/F was not significantly different across bins (p=0.084), but there was a significant difference among peak ACh activity bins (overall p<0.001, 3 vs 1 p=0.020, 3 vs 4 p=0.011, 4 vs 1 & 4 vs 2 p<0.001). d) Run onset-triggered ACh and axon activity binned by run duration speed (n=41-42 run periods). There was a significant difference in peak ΔF/F across bins for both axon activity (overall p=0.007, 1 vs 2 p=0.022, 1 vs 3 p=0.018, 1 vs 4 p=0.001) and ACh activity (overall p<0.001, 2 vs 3 p=0.025, 2 vs 4 p=0.002, 1 vs 2, 1 vs 3, & 1 vs 4 p<0.001). e) Time of peak ACh ΔF/F after peak axon ΔF/F for the run bins in D. There was a significant difference across bins (overall p<0.001, 2 vs 3 p=0.019, all other pairs p<0.001. Then, histogram of locations of peak axon vs ACh peri-run ΔF/F, expressed as a percentage of run (where 0% is run onset and 100% is run offset). Median peak axon ΔF/F occurred at 4.2% of the run, whereas median peak ACh ΔF/F occurred at 112.8% of the run. f) Dilation-triggered ACh and axon traces (n=1840 dilation periods). g) Dilation-triggered ACh and axon traces binned by dilation magnitude (n=460 dilations in each bin). There was a significant difference in median peak ΔF/F for both axon activity (overall p<0.001, all pairs except 2 vs 3 p<0.001) and ACh activity (overall p<0.001, 1 vs 2 p=0.005, all other pairs p<0.001).*

peaks in run-triggered axon and ACh activity was not consistent across groups. As run periods lasted longer, the peak in ACh activity occurred significantly later than the peak in axon activity for that same run period (Fig. 4e). Whereas axon activity typically peaked in about the first 4% of the run period, ACh activity did not reach its maximum until the very end of the run period. Overall, these results suggest that ACh levels may continue to increase under steady-state axonal release, potentially due to saturation of clearance mechanisms.

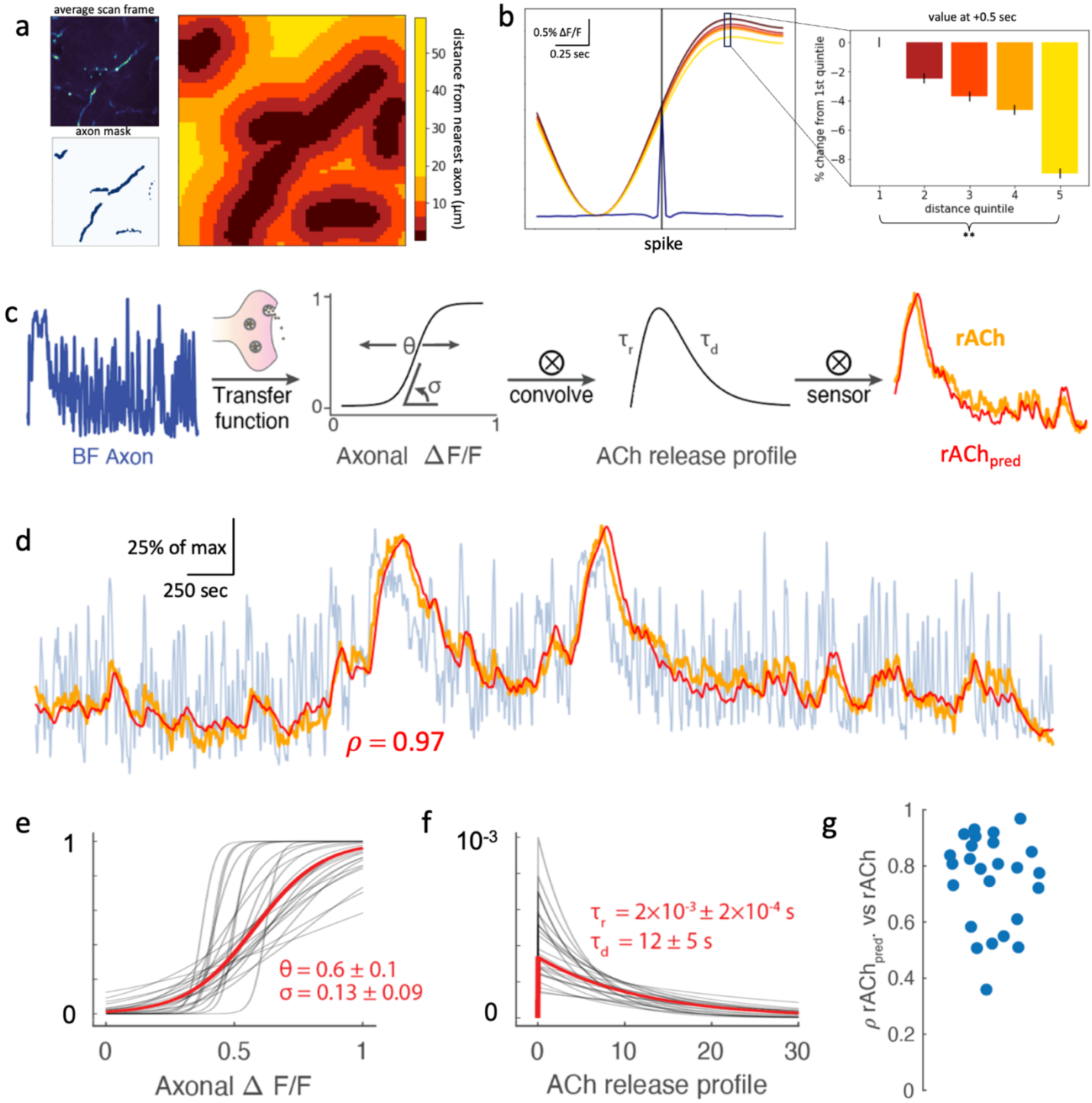

Figure 5: ACh activity decreases at distances further from an axon, and can be predicted temporally from cholinergic axon activity. *a) For one example scan, average scan frame, ROI mask representing location of axons, and a map representing pixel-wise distance from nearest axon as defined by the axon mask. B) Left: spike-triggered ACh ΔF/F for all scans averaged together (n=20,480 traces in each bin). Right: average ΔF/F value at 0.5 seconds after dilation expressed as percent change from the 1st quintile (i.e. the pixels closest to an axon). The rank order was significant (Spearman rank order correlation coefficient = -0.057, p<0.001). c) Prediction model workflow going from recorded cholinergic axon activity to predicted rACh signal. d) An example segment of recorded axon activity (blue), recorded rACh activity (orange), and predicted rACh activity (red). Pearson correlation $\rho = 0.97$ between recorded and predicted rACh. e) Sigmoidal activation function from axon activity to ACh release for each recording (black) and averaged over all recordings (red). f) ACh release functions for each recording (black) and averaged over all recordings (red). g) Pearson correlation between empirical and predicted rACh for each recording.*

We wondered if our imaging configuration would provide sufficient resolution to observe spatial features of local ACh release surrounding cholinergic axons. We did not necessarily expect to observe this effect with two-photon imaging, because we only monitored the activity of axons in a 2D plane (i.e. we were missing axons above and below the field of view). In each scan, we binned pixels according to distance from the nearest axon in the

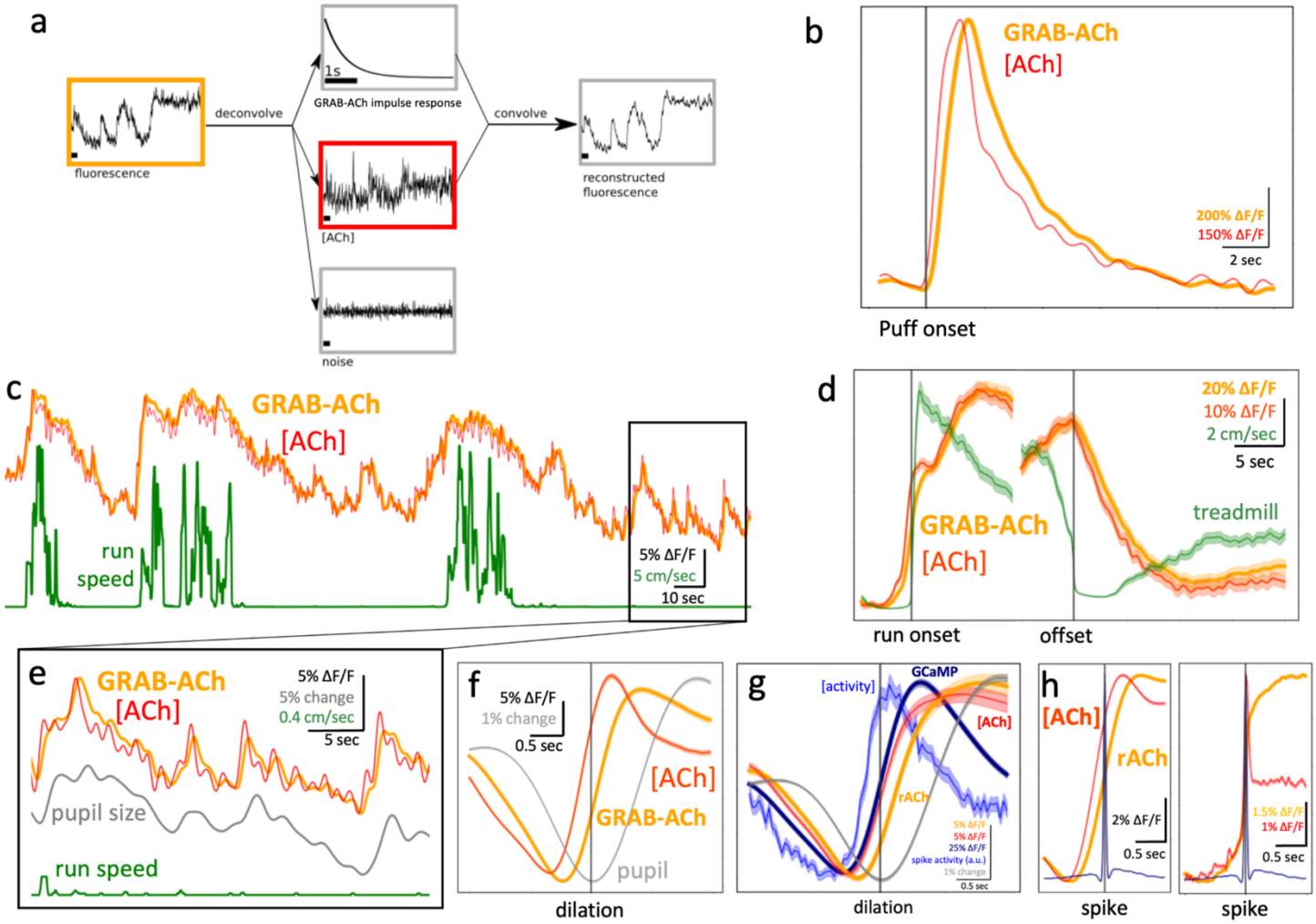

Figure 6: For small and fast events, GRAB-ACh deconvolution can help reveal rapid ACh kinetics. *a) Schematic illustrating the causal deconvolution filter. b) A single 100μM ACh injection-triggered GRAB-ACh trace with the deconvolved ACh trace overlaid. As expected, deconvolved ACh reaches a peak slightly before GRAB-ACh ΔF/F. c) An example trace of GRAB-ACh in VIS, along with deconvolved ACh and running trace. Deconvolution does not substantially alter the large-scale changes of ACh seen around running. d) Run onset- and offset-triggered GRAB-ACh and deconvolved ACh for all running periods in VIS recordings. Deconvolution does not significantly alter the timing of ACh increases before running or decay after running. e) Close-up of a quiescence period in the example traces in C, with the addition of pupil size. Deconvolution reveals sharper, more phasic activity of ACh correlated with spontaneous pupil size fluctuations. f) Dilation-triggered GRAB-ACh and deconvolved ACh traces for all dilation periods in VIS recordings. Deconvolved ACh rises and peaks sooner than is indicated by GRAB-ACh fluorescence. g) Dilation-triggered rACh and axon activity (GCaMP) with deconvolved ACh and axon activity traces. After deconvolution, the order of axon activity and ACh activity revealed in previous experiments is preserved. h) Spike-triggered GRAB-ACh and deconvolved ACh for all simultaneous axon-GRAB-ACh recordings (n=139,142 spikes; left, 1hz lowpass filtered; right, unfiltered). Again, deconvolved ACh rises and peaks sooner than what is indicated by GRAB-ACh fluorescence.*

field of view (example scan, Fig. 5a). Indeed, when looking at spike-triggered ACh in each of these spatial bins, weaker responses were observed in spatial bins further away from the nearest axon (Fig. 5b). The order of response magnitude from nearest to furthest bins was significant (Spearman's rank correlation coefficient = -0.057, $p<0.001$). This suggests that there is a small amount of spatial heterogeneity of ACh activity around cholinergic axons, consistent with a volume transmission mechanism.

In order to quantify the extent to which GRAB-ACh fluorescence fluctuations could be predicted from axon activity, we built a simple model with a sigmoidal function relating GCaMP axonal activity to ACh release, and an exponential rise (τ_r) and decay [32](τ_d; Fig. 5c) for ACh. We found that the dynamical framework was able to use axonal fluorescence (Fig. 5d, blue) to generate a prediction for rACh (Fig. 5d, red) that closely resembled

empirically measured rACh (Fig. 5d orange; Pearson correlation ρ = 0.97) between empirical and predicted rACh). Overall, we found the optimization algorithm predicted a slightly right-shifted sigmoidal (i.e., more calcium required for a response; Fig. 5e) and a rapid release ($\tau_r \sim 0$) with decay over seconds ($\tau_r \sim$12s, Fig. 5f). Across all recordings the algorithm could accurately predict rACh fluorescence ($\bar{\rho} = 0.8 \pm 0.2$; Fig. 5g) and explain a significant amount of the rACh variance ($\bar{\rho}^2 = 0.6 \pm 0.2$). This algorithm provides a simple method to use recordings of axonal fluorescence to predict what the GRAB-ACh sensor would report. More generally, it provides a strong validation for studies using cholinergic axon activity as a proxy for measuring local ACh levels in cortex, with the caveat that ACh levels and axon activity levels may be not be linearly related for large cholinergic events.

Having confirmed that cortical ACh levels track state-related variables and cholinergic axon activity, we wanted to better understand the actual time course of ACh fluctuations independent of GRAB-ACh sensor kinetics. We estimated the time course of [ACh] by deconvolving the fluorophore's impulse response from the fluorescence trace (Fig. 6a; see Supplementary Methods). Applying this deconvolution approach to an ACh puff-induced GRAB-ACh trace yielded the expected faster rise and return-to-baseline of [ACh] than the GRAB-ACh sensor (Fig. 6b). Large-scale ACh changes such as those surrounding running were too slow to be significantly affected by the sensor off time (Fig. 6c & d). However, deconvolution emphasized that the rapid clearance of smaller changes in ACh levels such as those triggered by pupil dilation may be somewhat obscured by the off kinetics of the GRAB-ACh sensor (Fig. 6e-h). Large-scale increases in ACh may lead to long-lasting availability of the neuromodulator, whereas small-scale increases may be very rapidly cleared. By chance, the sensor kinetics for GCaMP and rACh were similar enough that the lag between them was similar for de-convolved and non-deconvolved traces (Fig. 6g).

Finally, given our results indicating a close relationship between ACh and state-related behavior variables, we wondered how accurately we could predict ACh levels from these variables. To this end, we trained a long short-term memory (LSTM) recurrent neural network to predict GRAB-ACh fluctuations from the recorded behavioral dynamics – pupil size and running speed and their temporal derivative (Fig. 7a). The statistical model was able to reproduce the GRAB-ACh from training recordings ($\bar{\rho} = 0.7 \pm 0.2$; Fig. 7b), explaining over 50% of the GRAB-ACh variance ($\bar{\rho}^2 = 0.5 \pm 0.25$) both during high-arousal states marked by locomotion as well as quiescent states (Fig. 7a right). As expected, the model's explanatory capacity improved with an increase in correlation between the behavioral variables and GRAB-ACh signal, with model accuracy routinely exceeding behavioral signal by itself (Fig. 7c). Importantly, the model was able to correctly predict GRAB-ACh from behavior in unseen data (held-out validation dataset) at a performance matching training data (Fig. 7d left; explained-variance $\bar{\rho}^2 = 0.6 \pm 0.25$), indicating that it is general enough to be useful for predicting ACh levels from recordings without ground truth training data, i.e. in any head-fixed mouse experiment with recordings of treadmill and pupil size. As both behavioral variables are used as proxies for arousal, we wanted to contrast their explanatory power. Both behavioral measures independently led to a decrease in signal accuracy (Fig. 7d right both $p < 8 \times 10^{-6}$ paired t-test) and pupil size alone was significantly better than speed alone ($p < 0.05$ paired t-test). Overall, we have demonstrated that behavioral variables used to demarcate changes in brain state can also be used to predict ACh levels in the cortex.

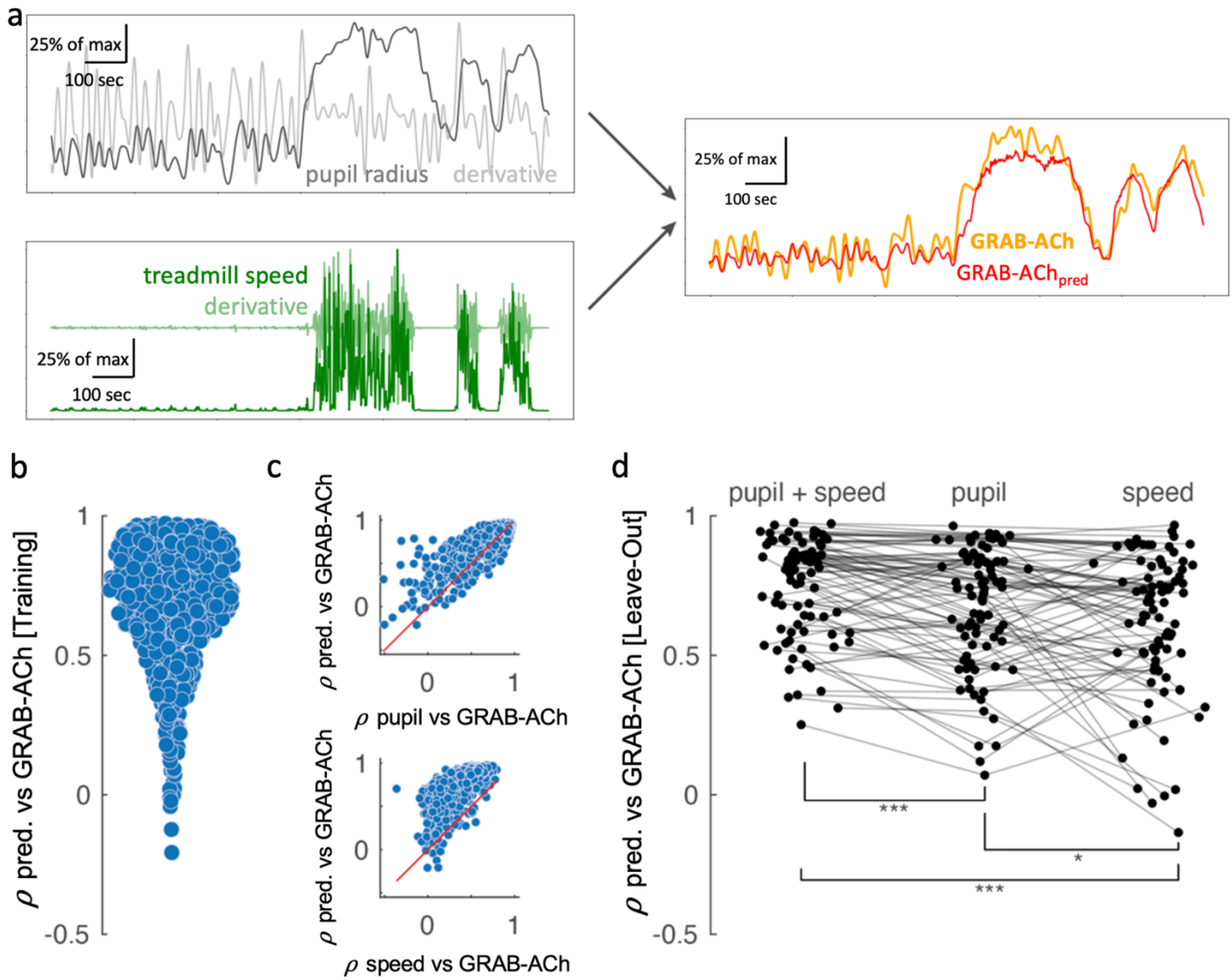

Figure 7: ACh levels can be predicted from pupil size and locomotion. *a) A model was constructed from pupil and treadmill measurements and their derivatives. Example traces of pupil radius/derivative and treadmill speed/derivative and the accompanying observed GRAB-ACh activity with predicted GRAB-ACh. b) Correlation between observed and predicted GRAB-ACh for each recording (training data). c) For each recording, correlation between pupil size and observed GRAB-ACh versus correlation between predicted and observed GRAB-ACh (top); the same comparison, but instead with treadmill speed. d) For the leave-out data, correlations between observed and predicted GRAB-ACh when using as prediction variables pupil size and treadmill speed together, or either of these two variables alone.*

DISCUSSION

We focused on spontaneous state changes and, consistent with previous work[21,23,25,26], we found that transitions from quiet wakefulness to the high-arousal state during locomotion resulted in a large increase in ACh which outlasts running periods by several seconds. Also consistent with previous results[24], ACh increases occurred around a half second before the onset of spontaneous epochs of pupil dilation that occur when animals are sitting quietly. We examined the relationship between the magnitude of behavioral state changes and the speed and magnitude of ACh release. While the timing of large-scale ACh increases were largely independent of running speed and duration, the timing of small-scale ACh increases did change in relation to the magnitude of the corresponding pupil dilation. In regards to the question over whether or not there is positive association between run speed and ACh response, past studies have had mixed results[21,23]. Here, we found that faster and longer run periods do indeed result in a larger ACh response. Differences in findings could be due to the exact time point where ACh is measured relative to running speed, since our results suggest that the peak in ACh

response occurs late in the running period (see below). Similarly, we found a clear positive association between pupil dilation magnitude and ACh response in our data, a point on which some studies differ[24,25].

While the basal forebrain is often referred to as a monolithic structure, evidence suggests it is actually somewhat modular with segregated projections to the cortex[33,34]. VIS receives a large proportion of its cholinergic projections from HDB, while the posterior nucleus basalis (NB) preferentially targets the auditory and anterior NB targets the SS[29]. A recent study[25] found heterogeneity in ACh responses across the dorsal cortex, specifically for run-triggered ACh. In contrast, we found that the magnitude and timing of large-scale run-evoked ACh was largely homogeneous across the dorsal cortical areas we examined, but our contrasting result may be due to differences in the way we computed these metrics or due to differences in experimental setup (e.g., one- vs. two-photon or differences in running measurements). On the other hand, we found that small-scale ACh increases – linked to pupil dilation – were larger in the visual cortex than in the more anterior cortical areas, and occurred with less of a delay relative to dilation.

We performed simultaneous measurements of cholinergic axons using GCaMP and the accompanying changes in ACh levels using a fluorescent ACh sensor. Broadly, we confirmed that local ACh levels do indeed increase in correspondence with axon activity as expected, and observed that the longer-lasting increases in ACh seen during running were much slower to decay than the rapid, phasic increases linked to dilation. This suggests that, in line with pharmacological studies indicating the rapid action of acetylcholinesterase (AChE)[35], small amounts of ACh are cleared quickly but larger increases may transiently saturate clearance mechanisms leading to longer decays[36]. We also found that cholinergic axon activity is more transient than ACh levels, and small increases in ACh fluorescence were accompanied by commensurate increases in cholinergic axon activity. However, large increases in ACh levels during longer and faster running periods occurred without a corresponding change in peak axon activity. This suggests that axonal release may be saturated during these epochs and release may outpace clearance, leading to build-up in ACh levels for a fixed "maximum" activity in the cholinergic projections. Spatially, we found that ACh availability decreases with increasing distance from axons, consistent with volume transmission of ACh. There has been an ongoing debate about whether ACh can escape the synapse and influence receptors on other processes not directly synapsing onto a cholinergic axon[36,37]. Our finding that the magnitude of cholinergic spike-triggered ACh activity displays a distance-dependent relationship may represent the first direct observation of volume transmission in vivo.

Predictive modelling revealed that cholinergic axon activity and behavioral state variables, especially pupil size, can be used for accurate predictions of cortical ACh levels, explaining the majority of variance on held-out data. Pupil and treadmill activity is routinely recorded in many head-fixed mouse experiments, and so this model may be useful for inferring ACh fluctuations in the absence of ground truth training data. The close correspondence of pupil size and cortical ACh levels is surprising, as traditionally the locus coeruleus (LC) (and, by proxy, norepinephrine) is thought to be the system most closely linked to pupil size, and the anatomical pathway by which LC could control pupil size has been well-established[27]. Fluctuations in cortical ACh delivered via the basal forebrain may occur downstream of projections from LC to BF[38,39]. Further studies are needed to examine this possibility, but we hope that this study emphasizes the translational potential of pupillometry for inferring fast changes in ACh, and that fluctuations in pupil size in humans should not be considered proxies for noradrenergic activity alone.

Our study provides a bridge between previous work using cholinergic axonal GCaMP imaging and recently-developed genetically encoded fluorescent sensors, and provides additional validation of GRAB-ACh for investigating the question of when and where ACh is available in the brain. The deconvolution approach we demonstrate here may be useful for other situations where it is desirable to estimate the time course of changes in levels of a ligand while removing the temporal smoothing due to slow sensor kinetics. Overall, these experiments contribute to a growing understanding of the spatiotemporal scale of ACh availability in the cortex in relation to state-related behavioral variables. This understanding is essential for future work focused on studying the downstream effects of ACh in changes on cortical excitability and information processing during perception and behavior.

METHODS

Animals, surgery, and injection of viral vectors

All procedures were carried out in accordance with the ethical guidelines of the National Institutes of Health and were approved by the Institutional Animal Care and Use Committee (IACUC) of Baylor College of Medicine. This study used a total of 32 mice aged 1.5 to 8 months (n=14 male, n=18 female).

Surgical procedures for spontaneous-state-change experiments and ACh injection experiments

Wild type C57Bl/6 mice (or various other negative genotypes on a C57Bl/6 background) were implanted with a 4mm cranial window over visual cortex (n=22), a 5mm window spanning visual and somatosensory cortices (n=3), or a 3mm window over motor cortex (n=2) under isoflurane anesthesia. The head was shaved over the dorsal portion of the skull and bupivacaine 0.25% (0.1 ml) and ketoprofen (5 mg/kg) were administered subcutaneously. The skin was pulled back and glued in place using Vetbond (3M). A headbar (steel washer with outer diameter 0.438", inner diameter 0.314", thickness 0.016") was affixed to the skull using dental cement (C&B Metabond). A micromotor rotary drill (Foredom) fitted with a 0.6mm tungsten carbide bur was used to thin the skull over the center of the chosen cortical area, which was determined by stereotactic coordinates (VIS: 2.8 mm lateral, 1mm anterior lambda; SS: 2.8mm lateral, 2.25mm posterior bregma; MO: 1.5mm lateral, 1mm anterior bregma), and a circle of skull was removed. A borosilicate glass pipette (World Precision Glass) was pulled to a tip width of 40µm and attached to a syringe which was used to inject 200-2000nl of AAV-hSyn-ACh4.3 at a depth of 200-700µm below the surface using a Micro4 MicroSyringe pump controller. The dura was removed and a #1 glass coverslip (thickness 0.15 ± 0.02 mm) was then glued in place using super glue (Loctite). The animal was allowed to recover in its home cage on a heated disk until sternal recumbency was regained, and was monitored for the next 3 days for signs of pain or distress.

Surgical procedures for dual axon-ACh imaging experiments

ChAT-cre (n=1) or Δneo ChAT-cre (n=4) mice first received an injection into the horizontal diagonal band (HDB) of the basal forebrain after anesthesia induction by i.p. Injection of ketamine and xylazine. HDB was selected due to its preferential cholinergic projections to the visual cortex[24,29,30]. The head was shaved and skin pulled back after an incision was made. A burr hole was drilled and, micropipette fitted with a 20µm glass pipette was positioned to AP: 0.13, ML: 1.1, DV: -5.6, and 1600nl of AAV-syn-FLEX-jGCaMP8s was injected over 160 seconds. The skin was sutured back in place using braided absorbable sutures (McKesson) and the animal allowed to recover. After 1 week, a headbar and 4mm cranial window was implanted over the visual cortex using the above procedures, into which 1000-1800nl of AAV-hSyn-rACh1.0 was injected at a depth of 300µm below the surface.

Locomotion and Pupillometry.

For all experiments, the mouse was positioned atop a 9"-diameter x 3"-wide cylindrical styrofoam treadmill and head-fixed using a steel headbar clamped onto the surgically-implanted washer. The surface of the treadmill was covered in duct tape to provide extra traction. The mouse's body was free to move with 2 degrees of freedom (forward and backward). An optical encoder (McMaster-Carr) was used to keep track of treadmill speed. Treadmill traces were processed with a 0.5 second median filter. Running periods were defined as running at a speed of least 1cm/sec for at least 1 second. Periods less than 3 seconds apart were grouped together into a single period.

A Dalsa camera mounted with a 55mm telecentric lens (OEM) and a 1" hot mirror (Thorlabs) was used to capture a video of the mouse's eye at 20fps. As the experiment was conducted in darkness with no visual stimulus, the eye was illuminated from an outside source (either a computer monitor at or a UV light) to prevent total pupil dilation and allow normal, spontaneous fluctuations in pupil size to be measured.

A DeepLabCut model was used to identify pupil edges from the eye videos, from which the circumference of the pupil was interpolated. The radius of the pupil (in pixels) was then determined, and this trace was 1hz lowpass filtered. Radius traces were inspected by eye to determine quality of tracking, and movies which had poor tracking were thrown out. To convert radius in pixels to radius in millimeters, the corners of the eyelid were detected using DeepLabCut and the median distance was assumed to be 2.757mm (which was determined by our measurements to be the universal mouse eyelid width). This was used to create a conversion factor whereby pixels could be converted to millimeters. Dilation (or constriction) events where then defined as periods of increasing (decreasing) pupil radius lasting greater than one second and with an average speed greater than 0.02mm/sec. Blinks or frames where the pupil was not able to be detected by DeepLabCut were considered NaNs, and any event comprised of more than 15% NaNs was dropped.

Imaging

All scans were recorded using a two-photon fast resonant scanning system (ThorLabs). Frame rates varied from 5-60fps. Excitation wavelengths were either 920nm (GRAB-ACh scans) or 1000nm (GCaMP and rACh scans) with a 25x objective (Nikon). Output power was kept around 15-40mW.

In vivo pharmacological experiments

In 4 mice under general isoflurane anesthesia, the glass coverslip previously implanted over the visual cortex was removed and replaced with a coverslip of the same size but with a small hole near the edge. The mouse was head-fixed under the microscope where it remained anesthetized for the duration of the experiment.

The following agents were diluted with cortex buffer and Alexa 568 dye to achieve specific molecular concentrations: acetylcholine chloride (crystals/powder, Sigma-Aldrich), norepinephrine bitartrate (crystalline, Sigma-Aldrich). A borosilicate patching pipette was fitted to a syringe and backfilled with the mixed pharmacological agent, and inserted into the cortex through the hole in the coverslip. 200 mBar pressure was applied to the syringe, which was released with a button press.

Preprocessing of imaging data.

All scans were corrected for motion in the X and Y directions via a two-step algorithm. Large scale motion was calculated by taking the average of the movie and computing phase correlation between this template and each frame of the movie. After correcting for large scale motion, smaller scale motion was corrected by taking the average of a 2,000 frame window and phase correlating frames within this window to the local template. Windows were selected to have 500 overlapping frames, and a linearly weighted average was taken for the displacement in the overlapping region.

For scans which recorded GRAB-ACh or rACh sensors, fluorescence traces were determined using a single ROI (mask) consisting of pixels which had average brightness values <99.9th percentile or and >99.9th percentile/2 or >99th percentile/2, respectively, after scan borders were removed (see Supplemental Fig. 2). The mask was then eroded using a 7x7-pixel kernel to provide smoothness. For scans which contained axons, a single mask was also determined for the green channel by calculating the overlap between manually-drawn mask over visible axons and a brightness mask. For scans where ACh was injected, a circular mask with 50µm radius was created over the tip of the injection pipette, which was manually defined.

Scans were discarded which had poor motion correction (defined as root-mean-squared of the x- and y-shifts produced from motion correction above 4 microns) or which contained large, unexplained jumps in fluorescence (at least 20x the average derivative). Three scans were discarded in which, despite adequate motion correction, it was assumed that the recorded axons moved out of the recording plane during motion due to a complete absence of detected spikes during running periods.

The first 20 seconds of each scan was thrown out in order to account for stabilization of the laser. The traces resulting from the above masks were detrended by subtracting a 4th-order polynomial to correct for photobleaching, 1hz lowpass filtered, and normalized from 0-1 to account for different raw fluorescence values across scans.

Hemodynamic artifacts are always a concern when recording bulk fluorescence with a sensor such as GRAB-ACh (although much less of a concern than with one-photon methods). We performed both 2-field (i.e., 2-ROI) and 2-channel controls with GRAB-ACh-mut and GRAB-ACh or rACh and found that qualitative differences were minor, and quantitative differences were only observed for the two-field correction (Supp. Fig. 3). When imaging two simultaneous fields, the differing vasculature patterns between the two sites could potentially lead to differences in artifact characteristics leading to an incorrect correction. When imaging two channels, the different fluorophores (red vs. green) could similarly contribute to differences in artifact characteristics. The signal-to-noise ratio of both GRAB-ACh and rACh was observed to be high, and thus we chose to use all GRAB-ACh and rACh traces "as-is" rather than attempting to apply a potentially imperfect hemodynamic correction method.

To determine spike times for peri-spike traces, the raw fluorescence calculated from the axon mask described above was deconvolved using a non-negative matrix factorization algorithm[40]. For each scan, a threshold was set at the 96th percentile of the deconvolved fluorescence values, and every sample point at or above this threshold was defined as a spike time. The threshold level was selected in order to achieve spiking rates which matched biologically-plausible firing rates of the cholinergic basal forebrain (approximately 4 spikes/sec overall[41] and approximately 7 spikes/sec during active periods[42]).

Peri-dilation, peri-run, and peri-spike traces.

The times at which dilations, run onsets, run offsets, or spikes occurred were determined using the methods above. The pre-processed fluorescence trace surrounding each event time was converted to ΔF/F by dividing by and then subtracting the average pre-event time fluorescence value ("baseline"). All peri-event ΔF/F traces were averaged together and standard error was found by dividing the standard deviation of all traces by the square root of the number of traces.

For distance-binned peri-spike traces, scans were spatially downsampled by a factor of 8 in order to reduce processing load. For each pixel, the distance in µm to the nearest pixel which contained an axon (as defined by the axon mask described above) was calculated. Distance bins were determined based on the distribution of distances across all scans. Peri-spike traces were then calculated for each bin using the method above.

GRAB-ACh deconvolution.

Fluorophore impulse response

Recent empirical work had characterized the GRAB-ACh sensor kinetics[23]; first used those results to model the fluorophore's impulse response (or convolution/deconvolution kernel) k. The exponential fall time had been directly determined to be $580ms$, by measurement of fluorescence in the presence of a competitive agonist. The inverse rise-time of the fluorescence response to an ACh puff increases logarithmically with molarity, with a constant $3.12/(\mu M \times s)$. However, as the convolution kernel is defined as the response to an instantaneous pulse of infinite concentration, and moreover because these are association kinetics (rather than kinetics of conformation state change in the fluorophore itself) by extrapolation the kernel's rise time should be effectively zero; we therefore modeled the kernel as a single falling exponential with time constant $580ms$.

Convolutional model

We then assumed (cf. Yaksi and Friedrich, 2006[43]) that the fluorescence signal is generated by convolution of a time-varying concentration $[ACh](t)$ with the fluorophore's impulse response k, so that the GRAB-ACh fluorescence trace $F(t)$ is:

$$F(t) = \int_{\tau} k(t-\tau)[ACh](t)d\tau$$

Roughly, the instantaneous concentration $[ACh]$ at time τ will cause a characteristic fluorescence response $k(t-\tau)$ --- which lasts for some time after fluorophores are activated. Contributions from fluorophores so activated at various times in the past (i.e., $t-\tau$) are then integrated to generate the fluorescence at time t. Note that this model does not account for nonlinear effects, in particular saturation.

Deconvolution

Deconvolution methods then attempt to invert the process of convolution, recovering the source $[ACh]$ from the fluorescence signal and the impulse response of the fluorophore. The simplest deconvolution method divides the Fourier transform (denoted $\mathcal{F}$, with inverse transform $\mathcal{F}^{-1}$) of the fluorescence signal by that of the kernel:

$$[ACh] \propto \mathcal{F}^{-1}\left(\frac{\mathcal{F}(F(t))}{\mathcal{F}(k)}\right)$$

However, we found this approach led to estimates of $[ACh]$ which – at least at the level of individual scans -- were so noisy as to be uninterpretable.

More advanced deconvolution methods differ largely by their assumptions on source and noise, yielding a denoised estimate of a conditioned source. Several modern methods (see also the review[44]), for instance, deconvolve latent voltage spikes from calcium fluorescence[45]. In our study, however, we cannot assume *a priori* that acetylcholine concentration $[ACh]$ is sparse or spikelike. A classical approach --- Wiener deconvolution (which had also previously been applied, with some modification, in the calcium context[46]) --- yielded intelligibly denoised single-trial $[ACh]$ estimates without further source constraints, making it a suitable method for our purposes.

Wiener deconvolution modifies the division method above by adding a regularization parameter to the denominator:

$$[ACh] \propto \mathcal{F}^{-1}\left(\frac{\mathcal{F}(F(t))}{\mathcal{F}(k)+\lambda^2}\right)$$

We estimated this parameter λ based on empirical considerations: As it increases, the reconstructed signal first shows removal of higher-frequency noise, but then shows a flattening of the variation of interest at lower frequencies --- eventually approaching a constant value (See Supplementary video 1). To select an appropriate degree of smoothing for each individual scan, we first standardized the signal, then varied lambda until the absolute reconstruction error was 10% of its maximum (i.e. 10% of when the signal flattened completely). Although this 'optimal' value of lambda was slightly larger computed over entire scans vs. stationary-only periods ($p < 10^{-10}$; Wilcoxon test), the size of this difference was fairly small (mean: 11.3%).

Axonal to ACh predictive modelling.

The axonal to ACh predictive model related the axonal fluorescence (F) to the simultaneously recorded rACh signal. First, a sigmoidal function calculated the maximal axonal output, $S(F)$,

$$S(F) = \frac{1}{1 + e^{\left(-\frac{F-\theta}{\sigma}\right)}},$$

where θ horizontally shifts the sigmoid (e.g., high $\theta \rightarrow$ smaller output S for given activity F) and σ is the rate of growth of the sigmoid from baseline to threshold. Next, we simulated the temporal release of ACh following an exponential rise and decay function by temporally convolving $S(F)$ with the release function $R(t)$,

$$R(t) = \frac{A\left(1 - e^{-\frac{t}{\tau_r}}\right) \times e^{-\frac{t}{\tau_d}}}{\sum_{t=t_{min}}^{t=t_{max}} \left(1 - e^{-\frac{t}{\tau_r}}\right) \times e^{-\frac{t}{\tau_d}}},$$

where τ_r and τ_d are the release rise and decay times, A is a scaling parameter, and the denominator is a normalization factor. Finally, the predicted ACh is convolved with the sensor dynamics $\left(1 - e^{-\frac{t}{\tau_{on}}}\right) \times e^{-\frac{t}{\tau_{off}}}$ (normalized to unit area) with $\tau_{on} = 153$ ms and $\tau_{on} = 580$ ms. The optimization swept across the 5 parameters $(\theta, \sigma, A, \tau_r, \tau_d)$ using an interior-point algorithm (MATLAB fmincon) over 150 iterations to minimize the RMSE between the predicted and empirically recorded GRAB-ACh signal.

Behavioral to ACh predictive modelling.

We predicted GRAB-ACh fluorescence from behavioral signals – running speed, pupil size and temporal derivatives – using a long short-term memory (LSTM) recurrent neural network. Briefly, the RNN consisted of an input layer, an LSTM layer (with a working memory of the previous ~ 8.5 s), a fully connected 256-node recurrent neural network, a 10% dropout layer, and a fully connected output layer. The model was trained on ~ 2-minute epochs across 90% of the recordings and validated on unseen held-out recordings (10% of total recordings). We optimized the parameters of the network through stochastic gradient descent using the Adam optimizer over 150 iterations, minimizing the RMSE between predicted and observed GRAB-ACh. The predictive model was trained using running speed, pupil size and their temporal derivatives (pupil + speed), pupil size and its temporal derivative (pupil), and running speed and its temporal derivative (speed). Model fits were assessed by calculating the Pearson correlation between predicted and observed GRAB-ACh in the held-out validation dataset.

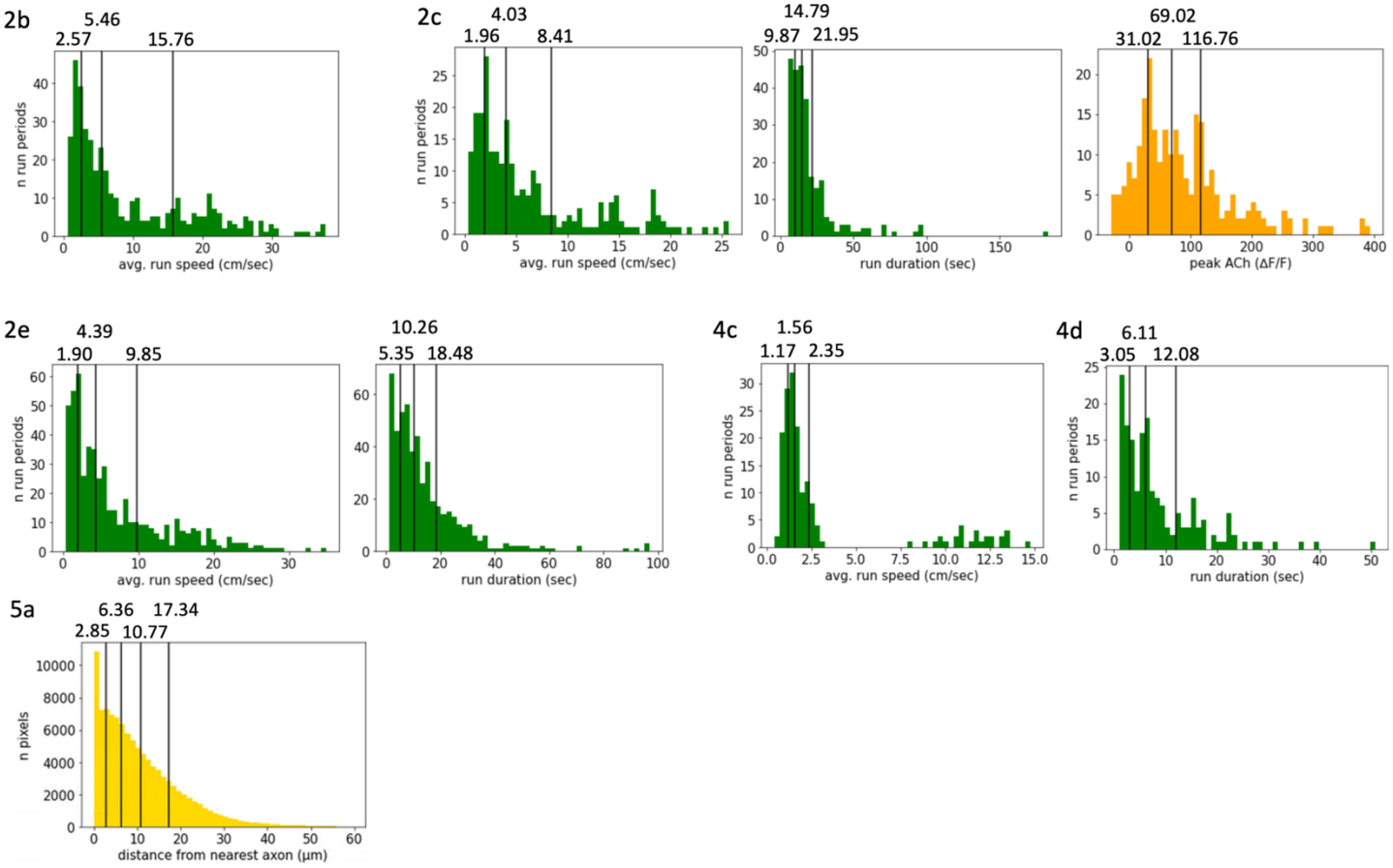

Supplementary Fig. 1 – Run qualities, peak ΔF/F, and distances per quartile/quintile for Figures 2, 4 & 5.

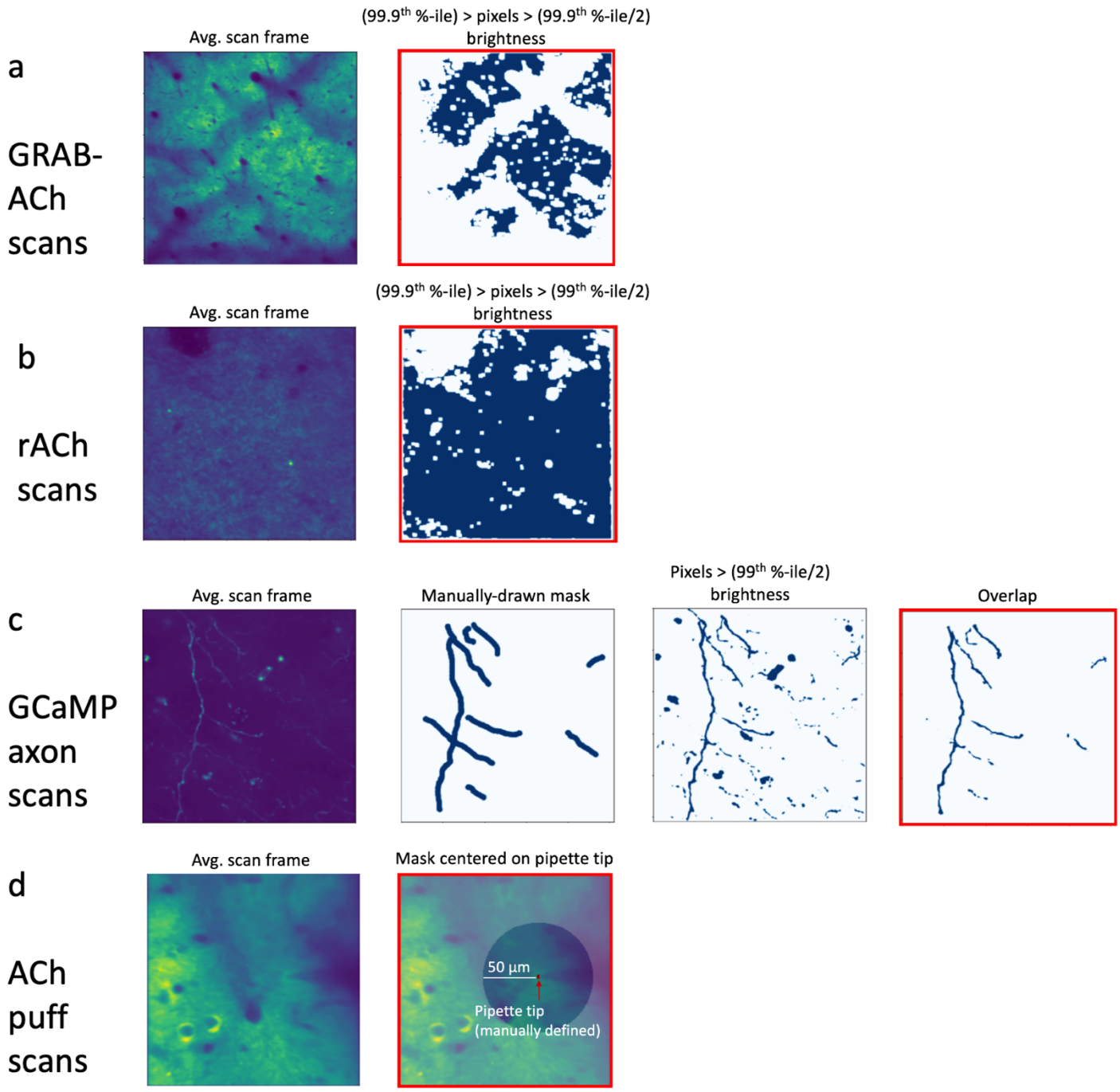

Supplemental Fig. 2 – Determination of ROIs. *In each panel, the red-boxed image was the final ROI used. a) Example average scan image and resulting mask for a GRAB-ACh scan. b) Example average scan image and resulting mask for an rACh scan. c) Example average scan image, the mask manually drawn over axons, the brightness mask, and the overlap of the two. d) Example average scan image and mask resulting from taking a 50µm radius around the manually-defined pipette tip.*

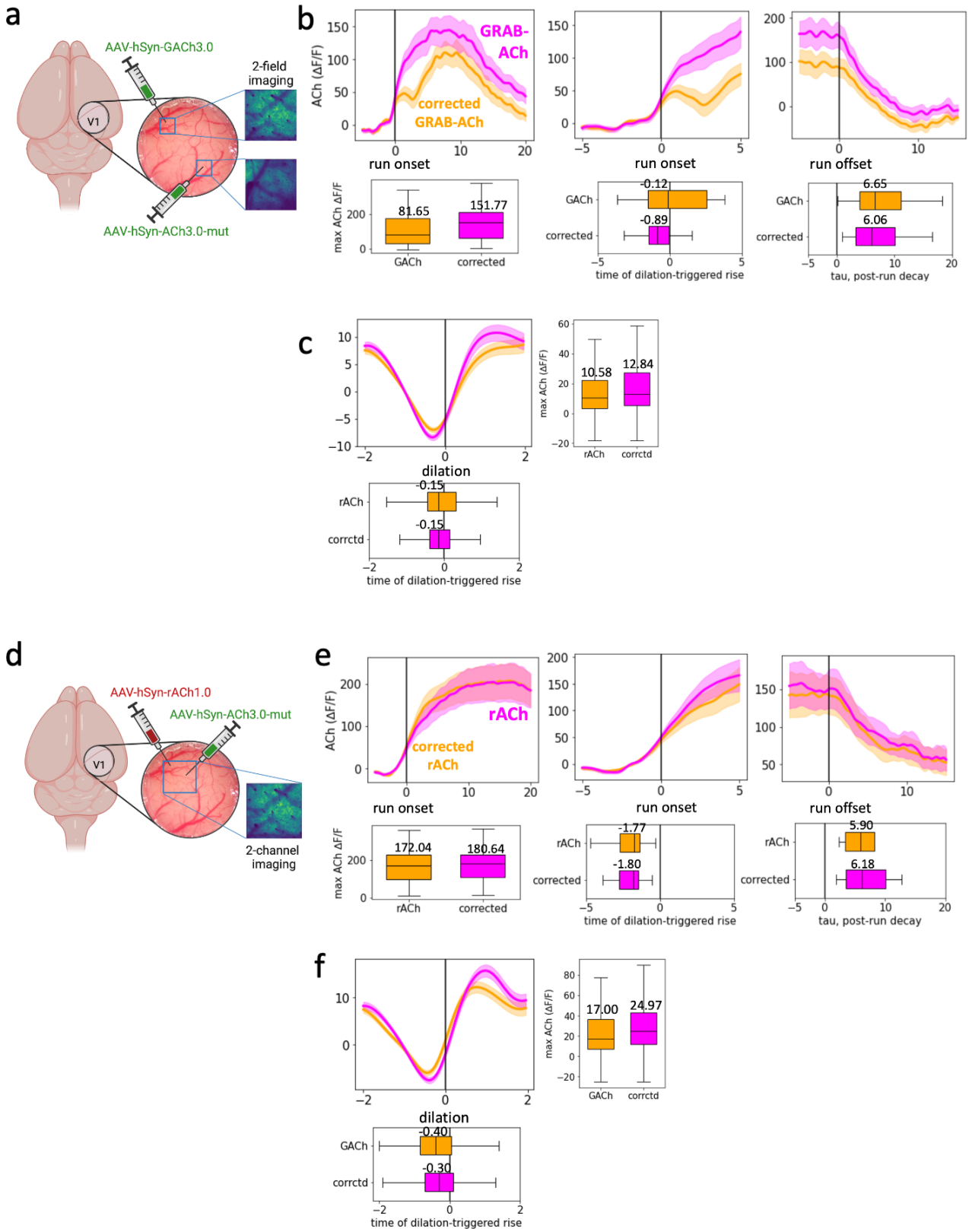

Supplemental Fig. 3 – Correcting for hemodynamic artifacts does not result in substantial differences in ACh. *a) A two-field imaging method to control for hemodynamic artifacts with GRAB-ACh. GRAB-ACh and GRAB-ACh-mut were expressed in spatially segregated areas of the same window and imaged simultaneously in different ROIs. The "corrected" trace was computed by adjusting the mean of the GRAB-ACh-mut trace to match the mean of the GRAB-ACh trace (outside of running periods), then subtracting this adjusted mut trace from the GRAB-ACh trace. b) Run onset- and offset-triggered GRAB-ACh and corrected GRAB-ACh with corresponding maximum response, rise onset time, and decay tau. c) Dilation-triggered GRAB-ACh and corrected GRAB-ACh with corresponding rise onset time and maximum response. d) A two-channel imaging method to control for hemodynamic artifacts with rACh. rACh and GRAB-ACh-mut were expressed in the same field and imaged simultaneously on different channels. The "corrected" trace was computed as in panel a. e) Run onset- and offset-triggered rACh and corrected rACh with corresponding maximum response, rise onset time, and decay tau. f) Dilation-triggered rACh and corrected rACh with corresponding rise onset time and maximum response. Panels a and d created with BioRender.com*

1. Reimer, J. Froudarakis, E., Cadwell, C. R., Yatsenko, D., Denfield, G. H. & Tolias, A. S. Pupil Fluctuations Track Fast Switching of Cortical States during Quiet Wakefulness. *Neuron* **84**, 355–362 (2014).
2. McGinley, M. J., David, S. V. & McCormick, D. A. Cortical Membrane Potential Signature of Optimal States for Sensory Signal Detection. *Neuron* **87**, 179–192 (2015).
3. Polack, P.-O., Friedman, J. & Golshani, P. Cellular mechanisms of brain state-dependent gain modulation in visual cortex. *Nat. Neurosci.* **16**, 1331–1339 (2013).
4. Bennett, C., Arroyo, S. & Hestrin, S. Subthreshold Mechanisms Underlying State-Dependent Modulation of Visual Responses. *Neuron* **80**, 350–357 (2013).
5. Aydın, Ç., Couto, J., Giugliano, M., Farrow, K. & Bonin, V. Locomotion modulates specific functional cell types in the mouse visual thalamus. *Nat. Commun.* **9**, 4882–12 (2018).
6. Mineault, P. J., Tring, E., Trachtenberg, J. T. & Ringach, D. L. Enhanced Spatial Resolution During Locomotion and Heightened Attention in Mouse Primary Visual Cortex. *J. Neurosci.* **36**, 6382–6392 (2016).
7. Erisken, S., Vaiceliunaite, A., Jurjut, O., Fiorini, M., Katzner, S. & Busse, L. Effects of Locomotion Extend throughout the Mouse Early Visual System. *Curr. Biol.* **24**, 2899–2907 (2014).
8. Vinck, M., Batista-Brito, R., Knoblich, U. & Cardin, J. A. Arousal and Locomotion Make Distinct Contributions to Cortical Activity Patterns and Visual Encoding. *Neuron* **86**, 740–754 (2015).
9. Dadarlat, M. C. & Stryker, M. P. Locomotion Enhances Neural Encoding of Visual Stimuli in Mouse V1. *J. Neurosci.* **37**, 3764–3775 (2017).
10. Tantirigama, M. L. S., Zolnik, T., Judkewitz, B., Larkum, M. E. & Sachdev, R. N. S. Perspective on the Multiple Pathways to Changing Brain States. *Front. Syst. Neurosci.* **14**, 23 (2020).
11. Metherate, R., Cox, C. & Ashe, J. Cellular bases of neocortical activation: modulation of neural oscillations by the nucleus basalis and endogenous acetylcholine. *J. Neurosci.* **12**, 4701–4711 (1992).
12. Williams, S. R. & Fletcher, L. N. A Dendritic Substrate for the Cholinergic Control of Neocortical Output Neurons. *Neuron* **101**, 486-499.e4 (2019).

13. Gill, D. F. & Hansel, C. Muscarinic modulation of SK2-type K^+ channels promotes intrinsic plasticity in L2/3 pyramidal neurons of the mouse primary somatosensory cortex. *eneuro* ENEURO.0453-19.2020 (2020) doi:10.1523/ENEURO.0453-19.2020.

14. Xiang, Z., Huguenard, J. R. & Prince, D. A. Cholinergic Switching Within Neocortical Inhibitory Networks. *Sci. Am. Assoc. Adv. Sci.* **281**, 985–988 (1998).

15. Nelson, A. & Mooney, R. The Basal Forebrain and Motor Cortex Provide Convergent yet Distinct Movement-Related Inputs to the Auditory Cortex. *Neuron* **90**, 635–648 (2016).

16. Collins, L., Francis, J., Emanuel, B. & McCormick, D. A. Cholinergic and noradrenergic axonal activity contains a behavioral-state signal that is coordinated across the dorsal cortex. *eLife* **12**, e81826 (2023).

17. Sturgill, J. F., Hegedus, P., Li, S. J., Chevy, Q., Siebels, A., Jing, M. & Li, Y. Basal forebrain-derived acetylcholine encodes valence-free reinforcement prediction error. http://biorxiv.org/lookup/doi/10.1101/2020.02.17.953141 (2020) doi:10.1101/2020.02.17.953141.

18. Eggermann, E., Kremer, Y., Crochet, S. & Petersen, C. C. H. Cholinergic Signals in Mouse Barrel Cortex during Active Whisker Sensing. *Cell Rep.* **9**, 1654–1660 (2014).

19. Zou, J., Trinh, S., Erskine, A., Jing, M., Yao, J., Walker, S., Li, Y. & Hires, S. A. Directed motor actions and choice signalling drive cortical acetylcholine dynamics. *bioRxiv* (2021) doi:10.1101/2021.12.21.473699.

20. Reimer, J., McGinley, M. J., Liu, Y., Rodenkirch, C., Wang, Q., McCormick, D. A. & Tolias, A. S. Pupil fluctuations track rapid changes in adrenergic and cholinergic activity in cortex. *Nat. Commun.* **7**, 13289 (2016).

21. Yogesh, B. & Keller, G. B. Cholinergic input to mouse visual cortex signals a movement state and acutely enhances layer 5 responsiveness. http://biorxiv.org/lookup/doi/10.1101/2023.06.07.543871 (2023) doi:10.1101/2023.06.07.543871.

22. Larsen, R. S., Turschak, E., Daigle, T., Zeng, H., Zhuang, J. & Waters, J. Activation of neuromodulatory axon projections in primary visual cortex during periods of locomotion and pupil dilation. http://biorxiv.org/lookup/doi/10.1101/502013 (2018) doi:10.1101/502013.

23. Jing, M., LI, Y., Zeng, J., Huang, P., Skirzewski, M., Kljakic., O., Peng, W., Qian, T., Tan, K., Zou, J., Trinh, S., Wu, R., Zhang, S., Pan, S., Hires, S. A., Xu, M., Li, H., Saksida, L. M., Prado, V. F., …, Li, Y. An optimized acetylcholine sensor for monitoring in vivo cholinergic activity. *Nat. Methods* **17**, 1139–1146 (2020).

24. Robert, B., Kimchi, E. Y., Watanabe, Y., Chakoma, T., Jing, M., Li, Y. & Polley, D. B. A functional topography within the cholinergic basal forebrain for encoding sensory cues and behavioral reinforcement outcomes. *eLife* **10**, e69514 (2021).

25. Lohani, S., Moberly, A. H., Benisty, H., Landa, B., Jing, M., Li, Y., Higley, M. J. & Cardin, J. A. Spatiotemporally heterogeneous coordination of cholinergic and neocortical activity. *Nat. Neurosci.* **25**, 1706–1713 (2022).

26. Borden, P. M., Zhang, P., Shivange, A. V., Marvin, J. S., Cichon, J., Dan, C., Podgorski, K., Figueiredo, A., Novak, O., Tanimoto, M., Shigetomi, E., Lobas, M. A., Kim, H., Zhu, P. K., Zhang, Y., Zheng, A. S., Fan, C. C., Wang, G., Xiang, B., …, Looger, L. L. A fast genetically encoded fluorescent sensor for faithful in vivo acetylcholine detection in mice, fish, worms and flies. http://biorxiv.org/lookup/doi/10.1101/2020.02.07.939504 (2020) doi:10.1101/2020.02.07.939504.

27. Joshi, S. & Gold, J. I. Pupil Size as a Window on Neural Substrates of Cognition. *Trends Cogn. Sci.* **24**, 466–480 (2020).

28. Bulumulla, C., Krasley, A. T., Cristofori-Armstrong, B., Valinsky, W. C., Walpita, D., Ackerman, D., Clapham, D. E. & Beyene, A. G. isualizing synaptic dopamine efflux with a 2D composite nanofilm. *eLife* **11**, e78773 (2022).

29. Kim, J.-H., Jung, A.-H., Jeong, D., Choi, I., Kim K., Shin, S., Kim, S. J. & Lee, S.-H. Selectivity of Neuromodulatory Projections from the Basal Forebrain and Locus Ceruleus to Primary Sensory Cortices. *J. Neurosci.* **36**, 5314–5327 (2016).

30. Huppé-Gourgues, F., Jegouic, K. & Vaucher, E. Topographic Organization of Cholinergic Innervation From the Basal Forebrain to the Visual Cortex in the Rat. *Front. Neural Circuits* **12**, 19 (2018).

31. Wu, L.-G. & Saggau, P. Presynaptic inhibition of elicited neurotransmitter release. *Trends Neurosci.* **20**, 204–212 (1997).

32. Shine, J. M. *et al.* Computational models link cellular mechanisms of neuromodulation to large-scale neural dynamics. *Nat. Neurosci.* **24**, 765–776 (2021).

33. Záborszky, L., Gombkoto., P., Varsanyi, P., Gielow, M. R., Poe, G., Role, L. W., Ananth, M., Rajebhosale, P., Talmage, D. A., Hasselmo, M. E., Dannenberg, H., Minces, V. H. & Chiba, A. A. Specific Basal Forebrain–Cortical Cholinergic Circuits Coordinate Cognitive Operations. *J. Neurosci.* **38**, 9446–9458 (2018).

34. Shine, J. M. Neuromodulatory Influences on Integration and Segregation in the Brain. *Trends Cogn. Sci.* **23**, 572–583 (2019).

35. Fuxreiter, M. & Warshel, A. Origin of the Catalytic Power of Acetylcholinesterase: Computer Simulation Studies. *J. Am. Chem. Soc.* **120**, 183–194 (1998).

36. Disney, A. A. & Higley, M. J. Diverse Spatiotemporal Scales of Cholinergic Signaling in the Neocortex. *J. Neurosci.* **40**, 720–725 (2020).

37. Sarter, M. & Lustig, C. Forebrain Cholinergic Signaling: Wired and Phasic, Not Tonic, and Causing Behavior. *J. Neurosci.* **40**, 712–719 (2020).

38. Vertes, R. P. Brainstem afferents to the basal forebrain in the rat. *Neuroscience* **24**, 907–935 (1988).

39. España, R. A. & Berridge, C. W. Organization of noradrenergic efferents to arousal-related basal forebrain structures. *J. Comp. Neurol.* **496**, 668–683 (2006).

40. Pnevmatikakis, E. A., Soudry, D., Gao, Y., Machado, T. A., Merel, J., Pfau, D., Reardon, T., Mu, Y., Lacefield, C., Yang, W., Ahrens, M., Bruno, R., Jessel, T. M., Peterka, D. S., Yuste, R. & Paninski, L. Simultaneous Denoising, Deconvolution, and Demixing of Calcium Imaging Data. (2017).

41. Xu, M., Chung, S., Zhang, S., Zhong, P., Ma, C., Chang, W.-C., Weissbourd, B., Sakai, N., Luo, L., Nishino, S. & Dan, Y. Basal forebrain circuit for sleep-wake control. *Nat. Neurosci.* **18**, 1641–1647 (2015).

42. Lee, M. G., Hassani, O. K., Alonso, A. & Jones, B. E. Cholinergic Basal Forebrain Neurons Burst with Theta during Waking and Paradoxical Sleep. *J. Neurosci.* **25**, 4365–4369 (2005).

43. Yaksi, E. & Friedrich, R. W. Reconstruction of firing rate changes across neuronal populations by temporally deconvolved Ca2+ imaging. *Nat. Methods* **3**, 377–383 (2006).

44. Evans, M. H., Petersen, R. S. & Humphries, M. D. On the use of calcium deconvolution algorithms in practical contexts. http://biorxiv.org/lookup/doi/10.1101/871137 (2019) doi:10.1101/871137.

45. Friedrich, J., Zhou, P. & Paninski, L. Fast online deconvolution of calcium imaging data. *PLOS Comput. Biol.* **13**, e1005423 (2017).

46. Holekamp, T. F., Turaga, D. & Holy, T. E. Fast Three-Dimensional Fluorescence Imaging of Activity in Neural Populations by Objective-Coupled Planar Illumination Microscopy. *Neuron* **57**, 661–672 (2008).